

**Identification of scintillation signatures on GPS signals originating from plasma structures detected with EISCAT incoherent scatter radar along the same line of sight**

Forte Biagio, Department of Electronic and Electrical Engineering, University of Bath, UK

Chris Coleman, Electrical and Electronic Engineering Department, The University of Adelaide, Australia

Susan Skone, Schulich School of Engineering, University of Calgary, Canada

Ingemar Häggström, EISCAT Scientific Association, Kiruna, Sweden

Cathryn Mitchell, Federico Da Dalt, Tommaso Paniciari, Department of Electronic and Electrical Engineering, University of Bath, UK

Joe Kinrade, Department of Physics, Lancaster University, UK.

Gary Bust, Applied Physics Laboratory, Johns Hopkins University, USA

Corresponding author: Biagio Forte, Department of Electronic and Electrical Engineering, University of Bath, Bath, BA2 7AY, UK. (b.forte@bath.ac.uk)

**Key points:**

- EISCAT ISR beam co-aligned with GPS satellite line of sight
- Absence of large-to-small scale energy cascade in the auroral E and F regions
- Scintillation-inducing plasma gradients in the auroral E and F regions

This article has been accepted for publication and undergone full peer review but has not been through the copyediting, typesetting, pagination and proofreading process which may lead to differences between this version and the Version of Record. Please cite this article as doi: 10.1002/2016JA023271

## **Abstract**

Ionospheric scintillation originates from the scattering of electromagnetic waves through spatial gradients in the plasma density distribution, drifting across a given propagation direction. Ionospheric scintillation represents a disruptive manifestation of adverse space weather conditions through degradation of the reliability and continuity of satellite telecommunication and navigation systems and services (e.g. EGNOS). The purpose of the experiment presented here was to determine the contribution of auroral ionisation structures to GPS scintillation. EISCAT measurements were obtained along the same line of sight of a given GPS satellite observed from Tromso and followed by means of the ESCAT UHF radar to causally identify plasma structures that give rise to scintillation on the co-aligned GPS radio link. Large-scale structures associated with the northern edge of the ionospheric trough, with auroral arcs in the nightside auroral oval and with particle precipitation at the onset of a substorm were indeed identified as responsible for enhanced phase scintillation at L band. For the first time it was observed that the observed large-scale structures did not cascade into smaller-scale structures, leading to enhanced phase scintillation without amplitude scintillation. More measurements and theory are necessary to understand the mechanism responsible for the inhibition of large-to-small scale energy cascade and to reproduce the observations. This aspect is fundamental to model the scattering of radio waves propagating through these ionisation structures. New insights from this experiment allow a better characterisation of the impact that space weather can have on satellite telecommunications and navigation services.

## **Index Terms:**

Auroral ionosphere (2704), Radio wave propagation (6964), Space and satellite communication (6979), Ionospheric effects on radio waves (7944)

**Keywords:**

GPS, Scintillation, Incoherent Scatter Radar, EISCAT, Auroral arcs, Ionospheric trough

**Introduction**

The propagation of radio waves through drifting inhomogeneities in the spatial distribution of electron density may lead to degradation of the overall signal manifesting itself as fluctuations of the phase and amplitude components of the radio waves, a phenomena known as scintillation [Yeh and Liu, 1982, Aarons, 1982; Basu et al., 1999; Basu et al., 2001; Fremouw et al, 1978]. Scintillation represents a serious threat to satellite telecommunication as well as satellite navigation systems as it can disrupt a service entirely, resulting in increased errors and outages [Seo et al, 2011; Kintner et al., 2007; Skone et al, 2001; Skone and de Jong, 2000, Skone, 2001].

In the presence of scintillation the energy received at the antenna is lower than in the absence of scintillation, a consequence of the scattering by electron density inhomogeneities in the ionosphere. When radio waves scatter through electron density structures the wave energy is scattered away from the original propagation direction, leading to a lower signal being recorded at the receiving antenna.

The scattering of radio waves that leads to ionospheric scintillation is often classified into three distinct regimes: (a) weak scattering, (b) moderate-to-strong scattering and (c) strong scattering [Yeh and Liu, 1982; Booker and MajidiAhi, 1981].

In the case of weak scattering the propagation problem can often be approximated by means of a single phase changing screen containing a distribution of phase changes (as a consequence of variations onto the spatial distribution of the refractive index) to be superimposed on the incident wave front [Booker and MajidiAhi, 1981; Rino, 1979]. In the case of moderate-to-strong scattering the use of multiple phase screens becomes necessary to

accommodate larger and cumulative phase variations in response to propagation through electron density structures with greater extent [Knepp, 1983; Uscinski, 1968; Carrano et al., 2011]. However, multiple phase screens should be placed with separations no more than the correlation length of the electron density structures, to properly reproduce strong scattering (i.e. as opposite to the distance effect).

The correlation length of plasma structures that gives rise to strong and saturating scintillation is hard to establish. Previous studies at low latitudes demonstrated that strong scintillation occurs in the vicinity of plasma bubbles walls as well as in the presence of plumes of ionisation [Rodrigues et al, 2004; Sripathi et al, 2008; Lee et al. 2009; Costa et al, 2011; Carrano et al., 2012; Patra et al., 2014]. At high latitudes strong scintillation is caused by the presence of plasma patches and particle precipitation [Skone et al, 2001; Mitchell et al, 2005; Forte, 2005; Smith et al., 2008; Prikryl et al., 2010; Kinrade et al., 2012; Kinrade et al., 2013; van der Meeren et al., 2014; van der Meeren et al., 2015]. In the case of satellite signals the propagation geometry is to be properly accounted for in the propagation problem together with the aspect ratio of electron density structures which signals need to traverse. In the case of GPS signals at high latitudes the propagation occurs at a significant angle to the magnetic field lines, along which plasma structures tend to elongate [Forte and Radicella, 2004].

The purpose of the experiment reported here was to provide insights into the type of structures that originate scintillation on GPS signals at auroral latitudes. In particular, the identification and characterisation of plasma gradients responsible for certain levels of scintillation was attempted by maintaining the EISCAT UHF radar along the same line of sight as a given GPS satellite (the signal recorded by means of a GPS scintillation monitor co-located with EISCAT UHF transmitter at Tromsø). The measurements described here were also utilised in a companion paper [Chartier et al., 2016], which focussed on the modelling of the scintillation observations by means of a propagation model based on 3-D

modelling of the propagation medium according to EISCAT electron density profiles. Optimum values of ionisations structures (e.g. outer scale and axial ratios) which provided the best fit to the observed scintillation were identified [Chartier et al., 2016]. Here, the identification and quantification of the contribution from E and F region irregularities to the observed L-band scintillation is provided through the combination of EISCAT and GPS observations under different circumstances.

### **Data and methodology**

The measurement campaign took place in October 2013 (see Table 1 for details), when different GPS satellites were followed with the EISCAT UHF radar during these measurements. Here, events from 16 October 2013 and 17 October 2013 only are reported.

The positions of GPS satellites to be followed were determined in advance on the basis of the projection of the ephemeris in the future by using a SP3 file ([http://igscb.jpl.nasa.gov/igscb/data/format/sp3\\_docu.txt](http://igscb.jpl.nasa.gov/igscb/data/format/sp3_docu.txt)) released the day before each of the days during the measurement campaign. Those positions were determined at 5 minute intervals to cover the entire duration of the measurement [Forte et al., 2013].

The EISCAT UHF radar was pointed towards the selected satellite by remaining fixed in a given position (defined in terms of azimuth and elevation) for 5 minutes, then re-positioning into the new direction in the next interval, and so on (see Figure 1). At each fixed position the GPS satellite line of sight was moving and traversing the radar line of sight in each 5-minute interval. During each 5-minute interval the radar was measuring and collecting backscattered power which was then converted into electron density profiles by using the typical GUISDAP analysis toolbox (<http://www.eiscat.com/groups/Documentation/UserGuides/GUISDAP/>) [Huuskonen and Lehtinen, 1996]. EISCAT electron density profiles were subsequently

calibrated following standard procedure (see Forte et al. (2013) for further details). The spatial resolution of the EISCAT radar measurements is of the order of 2 km in range.

Co-located with the EISCAT radar was a Novatel GNSS Ionospheric Scintillation and TEC Monitor (GPStation-6, <http://www.novatel.com/products/scintillation-tec-monitor/>) capable of measuring ionospheric parameters (i.e. TEC, rate of change of TEC, scintillation indices  $\sigma_\phi$  and  $S_4$ ) at 1-minute intervals as well as signals phase and amplitude components at 50 Hz rate [Van Dierendonck et al., 1993].

Figure 2 shows measurements for the event on 17 October 2013, while Figure 3 shows measurements for the event on and 16 October 2013. Figures 2 and 3 show electron density altitude profiles measured by EISCAT; scintillation indices corresponding to the GPS satellites followed by the EISCAT UHF radar, measured by means of the GPS scintillation monitor along a co-aligned direction; altitude profiles of the electric field calculated from the ion temperature and velocity following Banks and Kockarts (1973); altitude profiles of the ion temperature; power spectral densities (PSD) for de-trended carrier phase and for the normalised intensity of the GPS signals. PSDs were calculated over 3000 values at time covering an entire minute interval at 50 Hz sampling rate. Red stripes along the phase PSDs originated because of glitches generated by the GPS monitor clock.

In this experiment, the integration time of 60 seconds was chosen for the comparison with GPS scintillation indices (estimated over a 60-sec time interval) as well as to enhance sensitivity to smaller-scale electron density structures responsible for scintillation.

An integration time of 60 sec gave 5 different electron density profiles (one every 60 sec) along the same direction. The 5 different 60-sec profiles provided information on the

temporal evolution (e.g. energy cascade, drift, recombination) of the plasma structures detected (Figures 2 and 3).

An integration time of 60 sec implies a maximum spatial distance, between the radar direction and the offset satellite ray path at the beginning and end of a given 5-minute interval, of the order of 10 km in a direction transversal to the beam direction at about 200 km in altitude (and more at higher altitudes), assuming a GPS signal scan velocity of the order of 80 m/s at 200 km in altitude [Kaplan and Hegarty, 2006]. This provides an upper limit for the transversal spatial scales sampled by the GPS satellite signal, which together with electron density profiles provide information on the volume of ionisation structures originating particular scintillation signatures.

Components of the magnetic field are shown in Figure 4 (17 October 2013) and Figure 5 (16 October 2013) for the magnetometers at Ny Alesund (NAL), Hornsund (HOR), Bear Island (BJN), Tromso (TRO), Abisko (ABK), and Jackvik (JCK), part of the IMAGE network [Tanskanen, 2009].

## **Results**

### ***17 October 2013 PRN23 18 – 21 UT***

In the case of the measurements taken on 17 October 2013 (Figure 2), the EISCAT UHF radar detected several structures in the electron density profiles, some of which originating a corresponding signature on scintillation indices. Throughout the measurements, a peak in ionisation was around 300 km in altitude, with values of the order of  $2.5 \times 10^{11} \text{ el} \cdot \text{m}^{-3}$  on average and higher values between 18:50 and 19:30 UT and between 20:45 and 21:00 UT.

Between 18:00 and 18:30 UT some structures in the electron density profiles were detected below 200 km in altitude (extending less than 100 km in altitude each) with values of  $1.5 \times 10^{11} \text{ el} \cdot \text{m}^{-3}$  on average. These structures did not cause any remarkable signatures

neither on  $\sigma_\phi$  nor  $S_4$ , although a minor feature on  $S_4$  could be noticed at about 18:20 UT; no signatures could be identified on the intensity and phase PSDs (although phase PSDs were heavily masked by cycle slips in that time interval – Figure 2).

Between 18:30 and 19:00 UT another feature in the electron density profile (similar to those observed between 18:00 and 18:30) could be noticed (around 18:50 UT) which did not correspond to any signature on scintillation indices. The intensity PSDs did not show any modification while the phase PSDs showed an enhancement at lower temporal frequencies corresponding to the feature at 18:50 UT.

Between 19:00 and 19:30 UT three distinct electron density structures were detected with values of the order of  $2.5 \times 10^{11} \text{ el} \cdot \text{m}^{-3}$ , extending between 100 km and 200 km in altitude and within 10 km along the apparent GPS satellite direction across the radar line of sight (assuming an apparent satellite ray path scan velocity of 80 m/s at 200 km of altitude) over a background ionisation below  $1 \times 10^{11} \text{ el} \cdot \text{m}^{-3}$ . Around 300 km in altitude, the electron density intensified to about  $2.5 \times 10^{11} \text{ el} \cdot \text{m}^{-3}$  as well. Enhancements on phase PSDs at lower temporal frequencies were noticed in correspondence of these electron density structures, although only the first two of them originated a signature on  $\sigma_\phi$  (about 0.1 rad), leaving intensity PSDs and  $S_4$  unmodified. The spectral modifications noticed on the phase PSDs implied an enhancement at lower temporal frequencies and spectral broadening up to 0.6 Hz.

Between 19:30 and 20:00 UT no particular structures were detected by the radar and no particular signatures were observed either on the scintillation indices or on the PSDs.

Between 20:00 and 20:30 UT a first structure in electron density of about  $2.5 \times 10^{11} \text{ el} \cdot \text{m}^{-3}$  was detected followed by a more intense one of about  $3.5 \times 10^{11} \text{ el} \cdot \text{m}^{-3}$  on average, fading onto lower values afterwards. A volume of ionisation of about  $3.5 \times 10^{11} \text{ el} \cdot \text{m}^{-3}$  on average, extending between 100 km and 200 km in altitude and within 10 km along the

apparent GPS satellite direction across the radar line of sight over a background ionisation below  $1 \times 10^{11} \text{ el} \cdot \text{m}^{-3}$  was responsible for enhancing  $\sigma_\phi$  up to 0.45 rad (Figure 2). Spectral modifications were observed on the phase PSDs, with enhancement at lower temporal frequencies and spectral broadening up to 1 Hz. The intensity PSDs showed some enhancement above the Fresnel frequency as well as an increase in the Fresnel temporal frequency. After the most intense structure a sporadic E layer (diffuse aurora) established itself until 21:00 UT. Some structures in the electron density profiles of about  $1.5 \times 10^{11} \text{ el} \cdot \text{m}^{-3}$  and extending about 100 km in altitude were detected without any corresponding signature on either scintillation indices or PSDs.

Between 20:30 and 21:00 UT a sporadic E layer persisted with an intensification of electron density between 300 and 350 km in altitude, with values of the order of  $2.5 \times 10^{11} \text{ el} \cdot \text{m}^{-3}$  developing over apparently narrower layers.

During the whole interval of measurements, Tromsø was situated under the evening side of the auroral oval where auroral structures were frequently drifting. Changes in the electric field were observed as a consequence of polarisation electric fields [Aikio et al., 1993; de la Beaujardiere et al., 1977; Lanchester et al., 1996; Opgenoorth et al., 1990]. The abrupt ionisation enhancement detected between 20:00 and 20:30 UT coincided with a substorm onset (Figures 2 and 4) which was responsible for the associated particle precipitation. The timing of the features observed through co-aligned radar and GPS measurements are consistent with signatures observed through magnetometer data [Tanskanen, 2009]. The classical negative H (N-S) perturbation is indeed characteristic of auroral substorm onset at approximately 20:06 UT and associated energetic electron precipitation in the E region.

### **16 October 2013 PRN32 15-18 UT**

In the case of the measurements taken on 16 October 2013 (Figure 3), the EISCAT UHF radar beam detected some structures in the electron density distribution, responsible for enhancements in the phase scintillation index. Throughout the measurements, the F-region daytime peak in ionisation was noticeable between 200 and 400 km in altitude, with values of the order of  $3 \times 10^{11} \text{ el} \cdot \text{m}^{-3}$  on average between 15:00 and 15:45 UT. Then, the radar beam traversed a gap in the F region electron density between 15:45 and 16:30 UT, due to the transition between day side and night side. Subsequently, more ionisation in the F region was encountered with values of the order of  $1.5 \times 10^{11} \text{ el} \cdot \text{m}^{-3}$  until the end of that given satellite pass (at 18:05 UT). Moreover, a sporadic E layer was noticed after 16:00 UT.

Between 15:00 and 16:30 UT the radar transited from a daytime peak in the F region to the night side in such a time interval. The transition from the F-region daytime ionisation peak into the gap in electron density between 15:45 and 16:30 UT did not originate any enhancement on  $\sigma_\phi$  and  $S_4$  (Figure 3). No spectral modifications could be observed on both intensity and phase PSDs (Figure 3).

Between 16:30 and 17:30 UT the radar detected two distinct structures with values of the order of  $1.5 \times 10^{11} \text{ el} \cdot \text{m}^{-3}$ , extending between 100 km and 200 km in altitude and within 10 km along the apparent GPS satellite direction across the radar line of sight over a background ionisation below  $1 \times 10^{11} \text{ el} \cdot \text{m}^{-3}$ . The first of these structures was detected between 16:40 and 16:50 UT, while the second occurred between 17:20 and 17:30 UT. The first structure did enhance  $\sigma_\phi$  up to 0.3 rad in the same time interval, while the second structure caused a barely noticeable increase above the oscillator noise floor (i.e. 0.07 rad [Van Dierendonck et al., 1993]). Both these structures did not cause any appreciable signature on  $S_4$ . Phase PSDs were contaminated by clock glitches during this particular interval of measurements. Nevertheless, spectral modifications could be appreciated on the

phase PSDs, with enhancement at lower temporal frequencies and spectral broadening up to 1 Hz. The intensity PSDs showed some tenuous higher-frequency enhancement above the Fresnel frequency, in relation to these structures.

Between 17:30 and 18:05 UT the radar detected intensification in the F-region electron density at about 18:00 UT, with values increasing up to  $2.5 \times 10^{11} \text{ el} \cdot \text{m}^{-3}$  in some cases, extending between 200 km and 400 km in range. Scintillation indices were unmodified during this time interval.

Between 16:30 and 17:00 UT the northern edge of the ionospheric trough was passing over Tromsø, as indicated by the typical magnetic positive bay on the magnetic horizontal H component. Changes in the electric field were observed in correspondence of the ionospheric trough as a consequence of ionospheric convection [Moffett and Quegan, 1983; Roger et al., 1992]. After 17:00 UT, Tromsø was situated under the evening side of the auroral oval where auroral structures were frequently drifting (Figures 3 and 5).

## **Discussion**

Enhancements on the phase scintillation index  $\sigma_\phi$  were observed, corresponding to large-scale ionisation structures present along the GPS signal propagation direction (and co-aligned with the EISCAT UHF radar beam within the experiment accuracy). The presence of large-scale ionisation structures could be inferred from structures on the electron density profiles and corresponding enhancement of phase PSDs at lower temporal frequencies. In some cases, the enhancement was accompanied by spectral broadening up to 1 Hz (Figures 2 and 3). The large scale electron density structures introduced gradients in the refractive index distribution which in turn superimposed phase variations on the GPS signal propagating through. In general, the intensity scintillation index remained very small and constant throughout all of

the measurements and the PSDs of the normalised intensity did not show any distinct spectral modifications.

A possible explanation of these observations may be as follows. The low-frequency spectral enhancement on the PSD of the detrended GPS carrier phase, together with enhancements in the phase scintillation index  $\sigma_\phi$ , originate from large-scale auroral ionisation structures in the E and F regions. However, these large-scale ionisation structures did not cascade into smaller-scale structures (i.e. absence of enhanced amplitude scintillation). The inhibition of large-to-small scale energy cascade led to enhancements in phase scintillation without any enhancement in amplitude scintillation, when a fixed cut-off frequency is utilised to de-trend the carrier phase [Forte and Radicella, 2002]. The absence of an energy cascade to smaller scales could be due to higher recombination rates and/or strong conductivity along the field lines. Despite the fact that electron thermal diffusion can be a possible instability mechanism in the auroral E region plasma [Shalimov and Haldoupis, 1995], more measurements and theory are necessary to understand this issue and reproduce the observations. In particular, the observations would be reproduced by an instability mechanism that a) operates in the E-region of the ionosphere, b) injects free energy at larger scales and c) does not allow for an energy cascade to smaller scales.

From the comparison between electron density profiles and co-aligned scintillation indices it is evident that the scintillation was induced by ionisation structures in both E and F regions. However, the causal relationship between ionisation structures, and corresponding scintillation, is hard to explain on the basis of Figures 2 and 3 alone.

In order to identify and quantify the causal relationship between scintillation and ionisation structures in the E and F regions, the model by Booker and MajidiAhi (1981) was invoked [Vats, 1981; Forte, 2008; Forte, 2012]. This model enables the estimation of scintillation that

develops during propagation through a thick medium characterised by a mean square fractional fluctuation of the ionization spatial density  $\overline{\left(\frac{\Delta N}{N}\right)^2}$ , a mean ionisation density  $N$ , and a slab thickness  $D$ . The propagation through such an ionisation layer introduces mean square phase fluctuations described by [Booker, 1981; Booker and MajidiAhi, 1981; Vats et al., 1981; Forte, 2008; Forte, 2012]:

$$\overline{(\Delta\phi)^2} = 4r_e^2 N^2 \overline{\left(\frac{\Delta N}{N}\right)^2} \lambda^2 L_0 D \sec \chi \quad (1)$$

where  $r_e$  is the classical electron radius,  $L_0$  is the outer scale,  $D$  is the layer thickness, and  $\lambda$  is the wavelength of the signal considered.

An expression similar to (1) was derived by Knepp (1983b) by assuming that the layer thickness is greater than the correlation length of the irregularities. Knepp assumed a three-dimensional ionisation power spectrum of the form  $K^{-4}$ , with irregularities infinitely elongated in a direction orthogonal to the propagation direction. In this case, the structure function was approximated by a quadratic, whose coefficients were directly related to the outer scale, the inner scale, and the electron density fluctuations [Knepp, 1983b].

For the current experiment, the scattering model (1) was used to deduce information about the plasma density irregularities that cause L-band scintillation. It enables (a) the identification of the ionospheric layers which cause scintillation and (b) the estimate of outer scale, correlation length, and axial ratio of the irregularities.

#### ***(a) Identification of the ionospheric layers that cause L-band scintillation***

Equation (1) can be reinterpreted in terms of the mean square Total Electron Content (TEC) fluctuation along a particular ray path  $\overline{(\Delta N_T)^2}$ , avoiding assumptions on  $L_0$  and  $D$ , by

invoking the autocorrelation function  $B_{\Delta N_T}(\vec{\rho})$  for  $\Delta N_T$  [Yeh and Liu, 1982; Forte, 2008; Forte, 2012] as:

$$\overline{(\Delta\phi)^2} = \lambda^2 r_e^2 B_{\Delta N_T}(0) = \lambda^2 r_e^2 \overline{(\Delta N_T)^2} \quad (2)$$

From the radar measurements  $\overline{(\Delta N_T)^2}$  can be estimated by integrating electron density profiles over the E and F regions respectively. Hence, the contribution to the phase fluctuations at L band corresponding to the E and F regions can be estimated according to (2). Figures 6 and 7 show temporal fluctuations of the radar electron density (i.e.  $\Delta N_T$ ) profiles integrated over the E (blue) and F (red) region (top plot).  $\overline{(\Delta N_T)^2}$  was used to estimate  $\overline{(\Delta\phi)^2}$  from a given layer according to equation (2). The normalised contribution to the overall phase fluctuations from the E (blue area) and the F (red area) region is shown in Figures 6 and 7 (middle plot). Because of co-alignment, the GPS  $\Delta N_T$  and phase scintillation index can be used to identify the origin of L band scintillation (bottom plot in Figures 6 and 7).

In the case of 17 October 2013, the radar TEC temporal fluctuations from the E region were larger and comparable to the fluctuations from the F region between 19:00-19:30 UT and 20:00-20:15 UT, with enhancements on the GPS phase scintillation index  $\sigma_\phi$ , on the low-frequency phase PSD, and on the GPS TEC temporal fluctuations. This was consistent with the fact that Tromso was situated under the nightside of the auroral oval with auroral structures frequently traversing the radar beam (and the co-aligned GPS ray path). The ionisation in the E region was higher and, hence, the contribution to phase fluctuations from the E region was higher. In particular, between 20:00-20:15 UT larger phase fluctuations

from both the E and F regions were consistent with particle precipitation occurring on the equatorward edge of the auroral oval at the onset of an auroral substorm (Figures 2 and 4).

The radar TEC temporal fluctuations and the 50-Hz GPS temporal fluctuations (Figure 6) indicate the source of phase fluctuations to be large-scale ionisation structures in the E and F regions during the periods 19:00 – 19:30 UT and 20:00 – 20:15 UT. After this, only structures in the F region have influence, despite the presence of a diffuse-aurora sporadic E layer. A loss of lock on L2 semi-codeless was observed between 20:00 – 20:15 UT (discontinuity on the GPS TEC temporal fluctuations).

The sporadic E layer (diffuse aurora) following between 20:15 and 21:00 on 17 October 2013 as well as the sporadic E layer noticed between 16:00 and 18:05 UT on 16 October 2013 did not produce any remarkable signature on TEC temporal fluctuations, phase PSDs, GPS carrier phase, or scintillation indices.

In the case of 16 October 2013, the radar TEC temporal fluctuations between 16:30-17:00 UT were dominated by ionisation structures in the F region, hence phase fluctuations were mainly arising from the F region. Large-scale structures in the F region caused enhancements on the GPS phase scintillation index  $\sigma_\phi$ , on the low-frequency phase PSD, and on the GPS TEC temporal fluctuations. This is consistent with the presence of the trough across the radar beam between 16:30-17:00 UT indicated by a positive bay on the magnetic horizontal component (Figure 5) and further confirmed through TEC maps (Figure 8) [Mitchell and Spencer, 2003]. At around 17:15 UT another enhancement in the radar TEC temporal fluctuations with a larger contribution from the E region occurred without a marked signature on the GPS signals. This is consistent with the fact that after 17:00 UT, Tromsø was situated under the evening side of the auroral oval where auroral arcs were frequently passing. Hence, ionisation in the E region increased producing more contribution to phase perturbations arising from the E region. As opposed to the previous case, this ionisation seemed to attain

lower levels and hence it introduced smaller phase fluctuations overall. The radar TEC temporal fluctuations and the 50-Hz GPS TEC temporal fluctuations (Figure 7) indicate the origin of phase fluctuations from large-scale ionisation structures in the F region (16:30-17:00 UT), in both the E and F regions (around 17:15 UT), and in the F region only afterwards.

**(b) Estimate of outer scale, correlation length, and axial ratio**

Assuming the description in (1),  $\sigma_{\Delta N} = \sqrt{\overline{\left(\frac{\Delta N}{N}\right)^2}}$  can be estimated through the radar electron density profiles. Moreover, assuming that the phase scintillation index measured through the GPS L-band signal is such that  $\sigma_{\phi}^2 = \overline{(\Delta\phi)^2}$  and that  $D \sec \chi \approx 200 \text{ km}$  (in view of the considerations above) then the outer scale along the propagation direction can be found by solving (1) for  $L_0$ . Figures 9 and 10 show estimates of various quantities: the measured GPS phase scintillation index  $\sigma_{\phi}$  (green),  $\sigma_{\Delta N}$  (black), the correlation length of ionisation structures (red) obtained from the radar electron density fluctuations, and  $L_0$  (blue).

The correlation length is confirmed to be always less than the assumed layer thickness, which justifies the use of a model such as (1) [Booker and MajidiAhi, 1981; Knepp, 1983a,b]. The GPS phase scintillation increased with  $\sigma_{\Delta N}$ , as expected. However, the outer scale values varied in response to the combination between  $\sigma_{\Delta N}$  and  $\sigma_{\phi}$ : enhancements in  $\sigma_{\phi}$  corresponded to an outer scale of the order of 2 km (with a correlation length of the order of 20 km) in the case of 17 October 2013 and of the order of up to 8 km (with a correlation length of the order of 30 km) in the case of 16 October 2013. This indicates that the assumption of infinitely elongated irregularities along a direction transverse to propagation is more appropriate in the case of 16 October 2013 (16:30 – 17:00 UT) when F-region large-scale ionisation was detected: the ionisation showed more structure developed in the

transverse plane, which seems to suggest axial ratios of the order of 10:10:1 for the trough. On the other hand, the assumption was less appropriate in the case of 16 October 2013 (after 17:00 UT) and 17 October 2013 (19:00 – 19:30 UT and 20:00 – 20:15 UT) when ionisation due to particle precipitation was detected between the E and F regions: the ionisation showed more structure field-line elongated than in the transverse direction, with axial ratios of the order of 1:1:10.

In Chartier et al. (2016), the best fit to the observed scintillation required an axial ratio of 1, which indicate difficulties in modelling phase-without-amplitude scintillation at auroral latitudes.

## **Conclusions**

The present analysis has identified and quantified for the first time a causal relationship between auroral ionisation structures (as measured by the EISCAT UHF radar) and scintillation on GPS signals (as measured on GPS radio links co-aligned with the radar beam). The EISCAT UHF radar was pointed in the line of sight of a given GPS satellite, the satellite signal being recorded by means of a GPS scintillation monitor co-located with EISCAT UHF transmitter at Tromso.

The experiment has provided new insights on the type of structures that cause scintillation on GPS L-band signals at auroral latitudes.

Large-scale ionisation structures extending between the E and F regions cause phase-without-amplitude scintillation on GPS L-band signals, in response to low-frequency enhancements on the PSD of the de-trended GPS carrier phase. The absence of modifications on the PSD of the GPS intensity indicate for the first time that these large-scale ionisation structures did not cascade into smaller-scale structures. Amongst all known mechanisms, the electron thermal

diffusion instability [Shalimov and Haldoupis, 1995] seems possible in the auroral E region plasma, but not capable to reproduce the observations.

The reason for observing phase scintillations without amplitude scintillations is due to an instability mechanism that injects free energy at the kilometre or larger scales, but does not allow for an inertial sub-range energy cascade down to scales below the Fresnel scale, and to the use of a fixed cut-off frequency for de-trending the GPS carrier phase [Forte and Radicella, 2002].

It remains to be understood exactly what physical mechanism is the cause of these observations: that is, a new instability mechanism that a) operates in the E-region of the ionosphere, b) injects free energy at larger scales and c) does not allow for an energy cascade to smaller scales. Hence, more measurements and new theory are necessary to understand this issue.

In this experiment, large-scale ionisation structures were associated with the northern edge of the ionospheric trough, with auroral arcs drifting across the radar beam on the nightside auroral oval, and with particle precipitation at the onset of a substorm. The experiment indicated axial ratios of the order of 10:10:1 for F-region irregularities associated with the trough and 1:1:10 for irregularities in the E and F region associated with particle precipitation.

Future experiments of the type described here will provide further information concerning the axial ratio of irregularities in the auroral ionosphere as well as on the structure function associated with them. These experiments will also provide more details on the mechanisms responsible for the inhibition of large-to-small-scale cascade as well as on the modelling of propagation conditions leading to phase-without-amplitude scintillation at auroral latitudes. It is intended to include additional observations (LOFAR and SuperDARN) in these future experiments in order to provide additional data concerning the structure of the ionospheric

irregularities. In addition, the improvement of the model for phase-without-amplitude scintillation at auroral latitudes, following on Chartier et al. (2016), will be investigated.

### **Acknowledgements.**

This study was supported through the UK EPSRC Grant EP/H003304/1. EISCAT measurement time was funded partly through the UK Natural Environment Research Council and partly through the EISCAT International Peer Review Process.

EISCAT is an international association supported by research organisations in China (CRIRP), Finland (SA), Japan (NIPR and STEL), Norway (NFR), Sweden (VR), and the United Kingdom (NERC).

During the measurement campaign and subsequent data analyses Federico Da Dalt and Tommaso Paniciari were supported through a Marie Curie Initial Training Network (TRANSMIT) within the 7th European Community Framework Programme under Marie Curie Actions.

The authors wish to thank the institutes maintaining the IMAGE Magnetometer Array.

EISCAT data are available through the Madrigal archive (<https://www.eiscat.se/madrigal/>).

The GPS data used in this study are collected and archived by the University of Bath and available on request for joint studies. The magnetometer data are available through the IMAGE archive (<http://space.fmi.fi/image/index.html>).

The authors wish to thank Dr. A. Rodger (Associate Editor) and an anonymous reviewer for suggesting improvements to this paper.

## References

Aarons, J. (1982): Global morphology of ionospheric scintillations, *Proc. IEEE*, 70 (4), 360-378.

Aikio, A. T., H. J. Opgenoorth, M. A. L. Persson, and K. U. Kaila, Ground-based measurements of an arc-associated electric field, *J. Atmos. Terr. Phys.*, 55, 797-808, 1993.

Basu S., K. M. Groves, J. M. Quinn and P. Doherty (1999), A comparison of TEC fluctuations and scintillations at Ascension Island, *J. Atmos. Sol.-Terr. Phys.*, 61, 1219-1226.

Basu Su., S. Basu, C. E. Valladares, H.-C. Yeh, S.-Y. Su, E. MacKenzie, P. J. Sultan, J. Aarons, F. J. Rich, P. Doherty, K. M. Groves and T. W. Bullett (2001), Ionospheric effects of major magnetic storms during the International Space Weather Period of September and October 1999: GPS observations, VHF/UHF scintillations, and in situ density structures at middle and equatorial latitudes, *J. Geophys. Res.*, 106(A12), 30389-30413.

Booker, H. G. (1981), Application of refractive scintillation theory to radio transmission through the ionosphere and the solar wind, and to reflection from a rough ocean, *J. Atmos. Terr. Phys.*, 43(11), 1215–1233.

Booker, H. G., and G. MajidiAhi (1981), Theory of refractive scattering in scintillation phenomena, *J. Atmos. Terr. Phys.*, 43(11), 1199–1214.

Carrano, C. S., K. M. Groves, R. G. Caton, C. L. Rino, and P. R. Straus (2011), Multiple phase screen modeling of ionospheric scintillation along radio occultation raypaths, *Radio Sci.*, 46, RS0D07, doi:10.1029/2010RS004591.

Carrano, C. S., K. M. Groves, and R. G. Caton (2012), The effect of phase scintillations on the accuracy of phase screen simulation using deterministic screens derived from GPS and ALTAIR measurements, *Radio Sci.*, 47, RS0L25, doi:10.1029/2011RS004958.

Chartier, A., B. Forte, K. Deshpande, G. Bust, and C. Mitchell (2016), Three-Dimensional Modeling of High-Latitude Scintillation Observations, *Radio Sci.*, 51, doi:10.1002/2015RS005889.

Costa, E., E. R. de Paula, L. F. C. Rezende, K. M. Groves, P. A. Roddy, E. V. Dao, and M. C. Kelley (2011), Equatorial scintillation calculations based on coherent scatter radar and C/NOFS data, *Radio Sci.*, 46, RS2011, doi:10.1029/2010RS004435.

de la Beaujardiere, O., R. Vondrak, and M. Baron, Radar observations of electric fields and currents associated with arcs, *J. Geophys. Res.*, 82, 5051, 1977.

Forte, B., and S. M. Radicella, Problems in data treatment for ionospheric scintillation measurements, *Radio Sci.*, 37(6), 1096, doi:10.1029/2001RS002508, 2002.

Forte, B., and S. M. Radicella (2004), Geometrical control of scintillation indices: What happens for GPS satellites, *Radio Sci.*, 39, RS5014, doi:10.1029/2002RS002852.

Forte, B. (2005), Optimum detrending of raw GPS data for scintillation measurements at auroral latitudes, *J. Atmos. Sol. Terr. Phys.*, 67, 1100–1109.

Forte, B. (2008), Refractive scattering evidence from multifrequency scintillation spectra observed at auroral latitudes, *Radio Sci.*, 43, RS2012, doi:10.1029/2007RS003715.

Forte, B. (2012), Analysis of strong ionospheric scintillation events measured by means of GPS signals at low latitudes during disturbed conditions, *Radio Sci.*, 47, RS4009, doi:10.1029/2011RS004789.

Fremouw, E. J., R. L. Leadabrand, R. C. Livingston, M. D. Cousins, C. L. Rino, B. C. Fair, and R. A. Long (1978), Early results from the DNA Wideband Satellite Experiment—Complex signal analysis, *Radio Sci.*, 13(1), 167–187.

Huuskonen, A. and M. Lehtinen (1996), General incoherent scatter analysis and GUIDAP error estimates valid for high signal strengths, *J. Atmos. Terr. Phys.*, 58(1-4), 435-464, doi:10.1016/0021-9169(95)00047-X

Kaplan E. and C. Hegarty (2006), *Understanding GPS: principles and applications*, Second Edition, Artech House Inc., Norwood, MA, USA.

Kinrade, J., C. N. Mitchell, P. Yin, N. Smith, M. J. Jarvis, D. J. Maxfield, M. C. Rose, G. S. Bust, and A. T. Weatherwax (2012), Ionospheric scintillation over Antarctica during the storm of 5–6 April 2010, *J. Geophys. Res.*, 117, A05304, doi:10.1029/2011JA017073.

Kinrade, J., C. N. Mitchell, N. D. Smith, Y. Ebihara, A. T. Weatherwax, and G. S. Bust (2013), GPS phase scintillation associated with optical auroral emissions: First statistical results from the geographic South Pole, *J. Geophys. Res. Space Physics*, 118, 2490–2502, doi:10.1002/jgra.50214.

Kintner, P. M., B. M. Ledvina, and E. R. de Paula (2007), GPS and ionospheric scintillations, *Space Weather*, 5, S09003, doi:10.1029/2006SW000260.

Knepp D. L. (1983a), Multiple phase-screen calculation of the temporal behaviour of stochastic waves, *Proc. IEEE*, 71(6), 722-737.

Knepp D. L. (1983b), Analytic solution for the two-frequency mutual coherence function for spherical wave propagation, *Radio Sci.*, 18(4), 535-549.

Lanchester, B. S., K. Kaila, I. W. McCrea, Relationship between large horizontal electric fields and auroral arc elements, *J. Geophys. Res.*, 101, 5075-5084, 1996.

Lee, C. C., F. D. Chu, W. S. Chen, J. Y. Liu, S.-Y. Su, Y. A. Liou, and S. B. Yu (2009), Spread F, GPS phase fluctuations, and plasma bubbles near the crest of equatorial ionization anomaly during solar maximum, *J. Geophys. Res.*, 114, A08302, doi:10.1029/2009JA014195.

Mitchell, C. N. and P. S. J. Spencer (2003), A three-dimensional time-dependent algorithm for ionospheric imaging using GPS, *Annals of Geophysics*, 46(4), 687-696.

Mitchell, C. N., L. Alfonsi, G. De Franceschi, M. Lester, V. Romano, and A. W. Wernik (2005), GPS

TEC and scintillation measurements from the polar ionosphere during the October 2003 storm, *Geophys. Res. Lett.*, 32, L12S03, doi:10.1029/2004GL021644.

Moffett, R. J., and S. Quegan, The mid-latitude trough in the electron concentration of the ionospheric F layer: a review of observations and modelling, *J. atmos. terr. Phys.*, 45, 315-343, 1983.

Opgenoorth, H. J., I. Häggström, P. J. Williams, and G. O. L. Jones, Regions of strongly enhanced perpendicular electric fields adjacent to auroral arcs, *J. Atmos. Terr. Phys.*, 52, 449-458, 1990.

Patra, A. K., P. Srinivasulu, P. P. Chaitanya, M. D. Rao, and A. Jayaraman (2014), First results on low-latitude E and F region irregularities obtained using the Gadanki Ionospheric Radar Interferometer, *J. Geophys. Res. Space Physics*, 119, 10,276–10,293, doi:10.1002/2014JA020604.

Prikryl P., P. T. Jayachandran, S. C. Mushini, D. Pokhotelov, J.W. MacDougall, E. Donovan, E. Spanswick, and J.-P. St.-Maurice (2010), GPS TEC, scintillation and cycle slips observed at high latitudes during solar minimum, *Ann. Geophys.*, 28, 1307-1316, doi:10.5194/angeo-28-1307-2010.

Rino, C. L. (1979), A power law phase screen model for ionospheric scintillation 1. Weak scatter, *Radio Sci.*, 14(6), 1135–1145.

Rodrigues, F. S., E. R. de Paula, M. A. Abdu, A. C. Jardim, K. N. Iyer, P. M. Kintner, and D. L. Hysell (2004), Equatorial spread F irregularity characteristics over São Luis, Brazil, using VHF radar and GPS scintillation techniques, *Radio Sci.*, 39, RS1S31, doi:10.1029/2002RS002826.

Roger, A. S., R. J. Moffett, and S. Quegan, The role of ion drift in the formation of the ionisation troughs in the mid- and high-latitude ionosphere - a review, *J. Atmos. Terr. Phys.*, 54, 1-30, 1992.

Seo J., T. Walter and P. Enge (2011), Availability Impact on GPS aviation due to strong ionospheric scintillation, *IEEE Trans. on Aerosp. and Electr. Syst.*, 47(3), 1963-1973.

Shalimov S. and C. Haldoupis (1995), An electron thermal diffusion instability and type-3 echoes in the auroral E-region plasma, *Ann. Geophys.*, 28, 45-55.

Skone S. and M. de Jong (2000), The impact of geomagnetic substorms on GPS receiver performance, *Earth Plan. Sp.*, 52, 1067–1071.

Skone S., K. Knudsen and M. de Jong (2001), Limitations in GPS receiver tracking performance under ionospheric scintillation conditions, *Phys. Chem. Earth (A)*, 26(6-8), 613-621.

Skone S. (2001), The impact of magnetic storms on GPS receiver performance, *J. Geod.*, 75, 457-468.

Smith, A. M., C. N. Mitchell, R. J. Watson, R. W. Meggs, P. M. Kintner, K. Kauristie, and F. Honary (2008), GPS scintillation in the high arctic associated with an auroral arc, *Space Weather*, 6, S03D01, doi:10.1029/2007SW000349.

Sripathi S., S. Bose, A. K. Patra, T. K. Pant, B. Kakad, and A. Bhattacharyya (2008), Simultaneous observations of ESF irregularities over Indian region using radar and GPS, *Ann. Geophys.*, 26, 3197–3213.

Tanskanen, E.I. (2009), A comprehensive high-throughput analysis of substorms observed by IMAGE magnetometer network: Years 1993-2003 examined, *J. Geophys. Res.*, 114, A05204, doi:10.1029/2008JA013682.

Uscinski, B. J. (1968), The multiple scattering of waves in irregular media, *Phil. Trans.*, A262, 609–640.

Valladares C. E., J. Villalobos, R. Sheehan, M. P. Hagan (2004), Latitudinal extension of low-latitude scintillations measured with a network of GPS receivers. *Ann. Geophys.*, 22 (9), 3155-3175.

van der Meer, C., K. Oksavik, D. Lorentzen, J. I. Moen, and V. Romano (2014), GPS scintillation and irregularities at the front of an ionization tongue in the nightside polar ionosphere, *J. Geophys. Res. Space Physics*, 119, 8624–8636, doi:10.1002/2014JA020114.

Van Dierendonck, A. J., Q. Hua, and J. Klobuchar (1993), Ionospheric scintillation monitoring using commercial single frequency C/A code receivers, paper presented at Sixth

International Technical Meeting of the Satellite Division of the Institute of Navigation GPS  
93, Salt Lake City, Utah, 22–24 Sept. 1993.

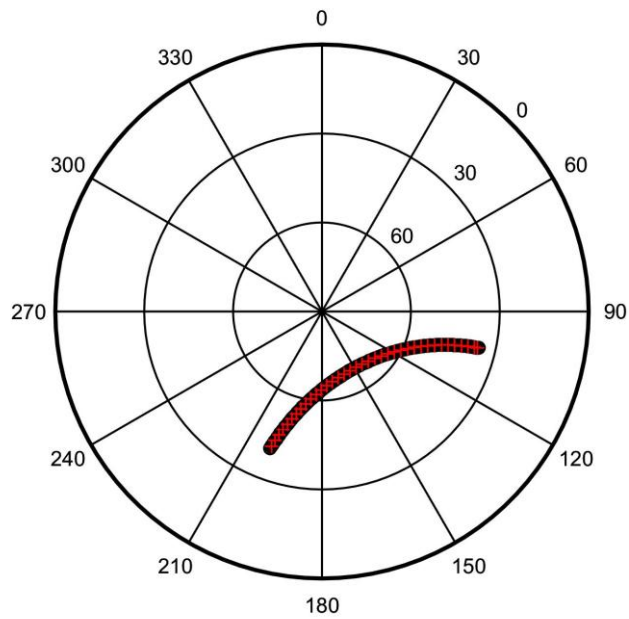
Vats, H. O., H. G. Booker, and G. MajidiAhi (1981), Quantitative explanation of strong  
multifrequency intensity scintillation spectra using refractive scattering, *J. Atmos. Terr.  
Phys.*, 43(12), 1235–1241.

Yeh, K. C., and C. H. Liu (1982), Radio wave scintillations in the ionosphere, *Proc. IEEE*,  
70(4), 324–360.

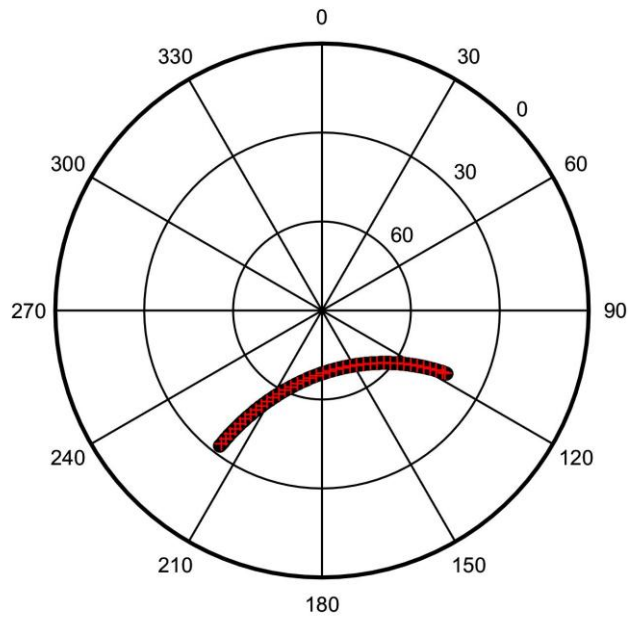
Accepted Article

**Table 1:** Summary of GPS satellites followed by the radar throughout the measurement campaign.

<b>Date</b>	<b>GPS Satellite Followed by the Radar</b>	<b>Time Interval (UT)</b>
07 October 2013	PRN22	14:00 – 15:45
	PRN32	15:50 – 18:45
	PRN23	18:50 – 21:00
16 October 2013	PRN19	14:00 – 14:55
	PRN32	15:00 – 18:05
	PRN23	18:10 – 21:00
17 October 2013	PRN23	18:00 – 21:00
18 October 2013	PRN11	14:00 – 15:30
	PRN32	15:35 – 17:55
	PRN23	18:00 – 21:00



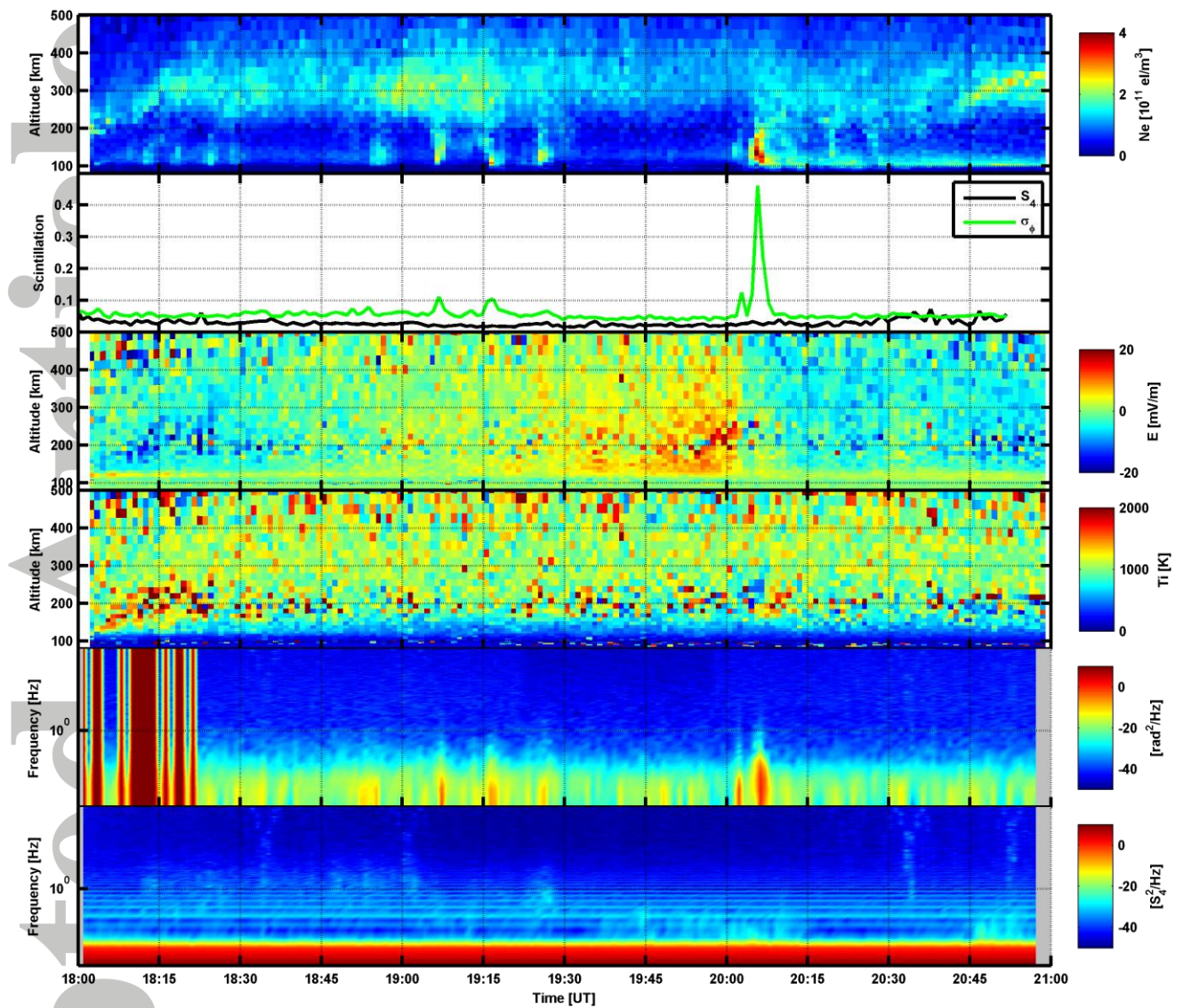
(a) 17 October 2013 PRN23



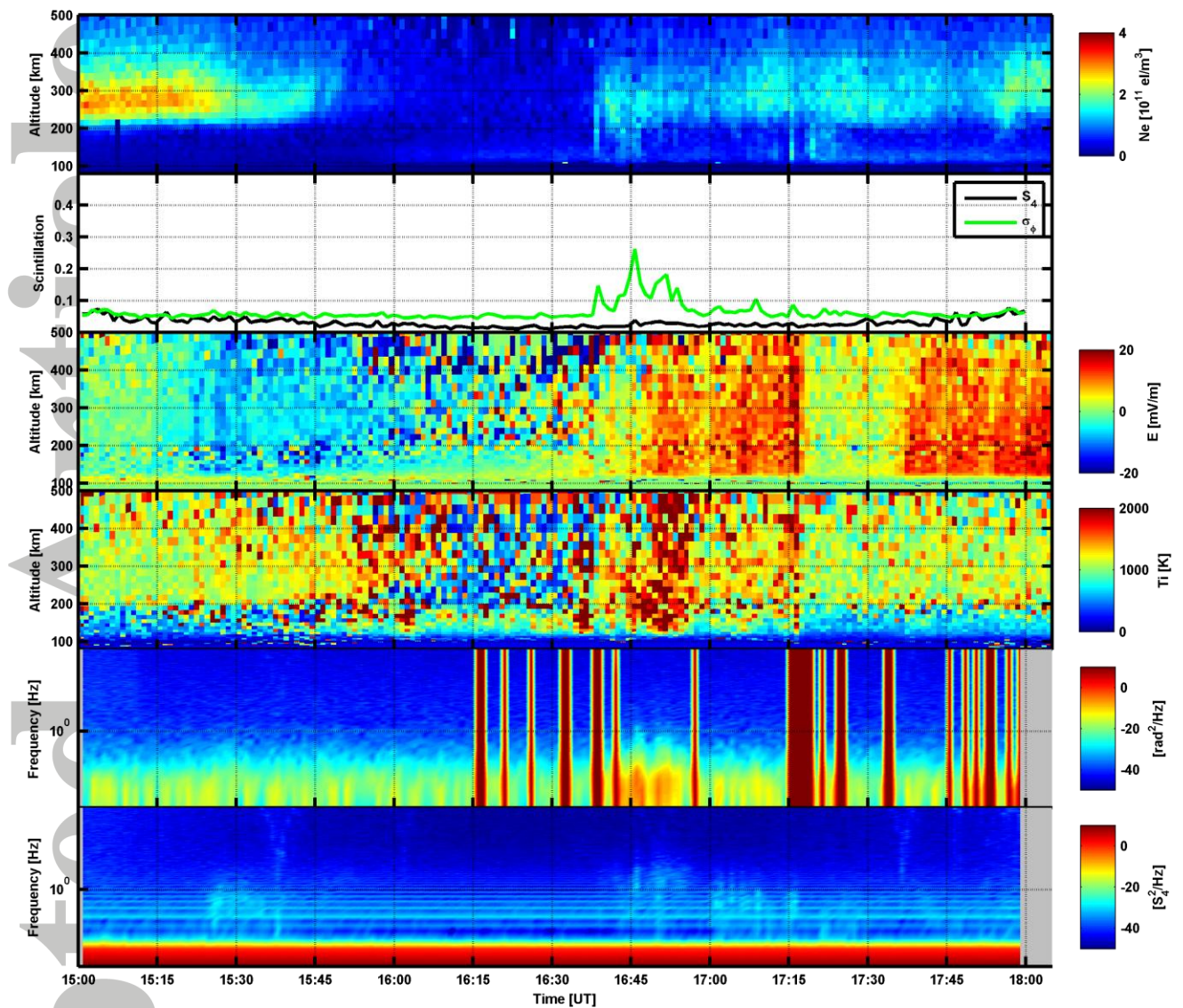
(b) 16 October 2013 PRN32

**Figure 1:** Trajectories of the GPS satellites (black circles) followed by the radar (red crosses), in terms of azimuth and elevation angles. The numbers over each of the black circles indicate the subsequent minutes within a given 5-minute interval. It can be seen that maximum alignment between nominal GPS line of sight and nominal radar beam occurred around minute 3 within each 5-minute interval.

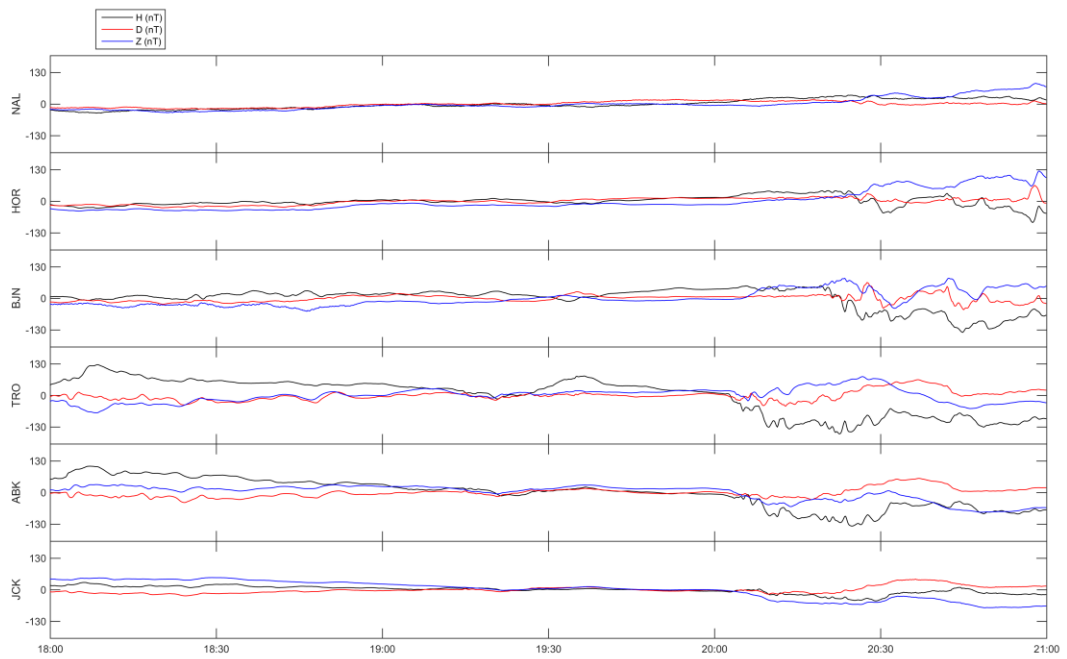
Accepted Article



**Figure 2:** The event measured on 17 October 2013, characterised by (from top to bottom) electron density profiles, GPS scintillation indices, electric field, ion temperature, PSD for the de-trended carrier phase and PSD for the normalised intensity.

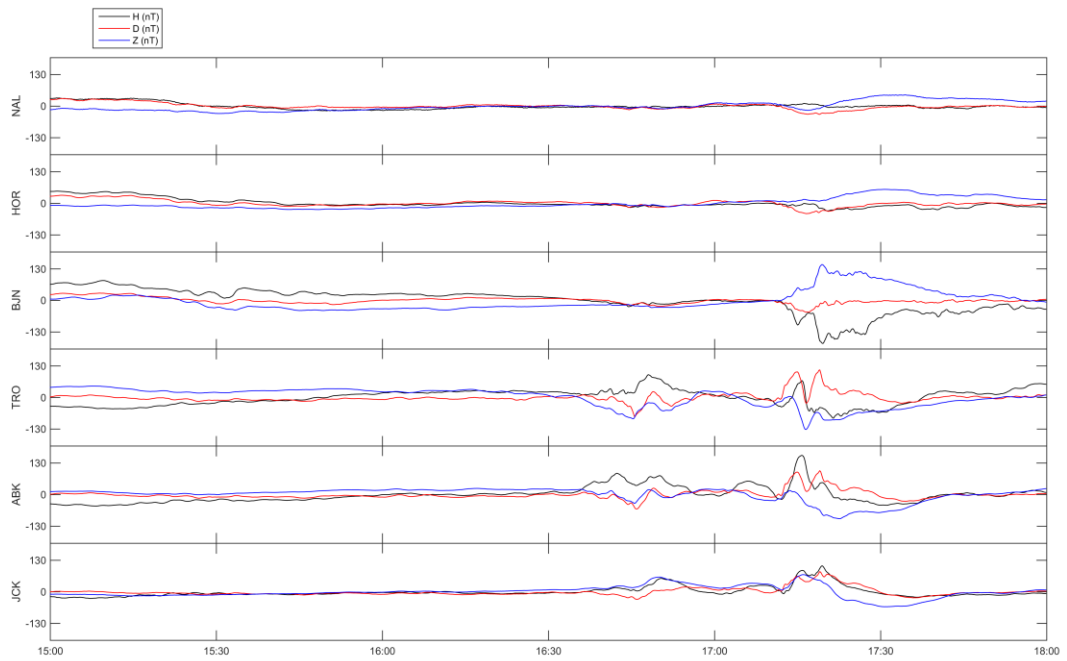


**Figure 3:** The event measured on 16 October 2013, characterised by (from top to bottom) electron density profiles, GPS scintillation indices, electric field, ion temperature, PSD for the de-trended carrier phase and PSD for the normalised intensity.



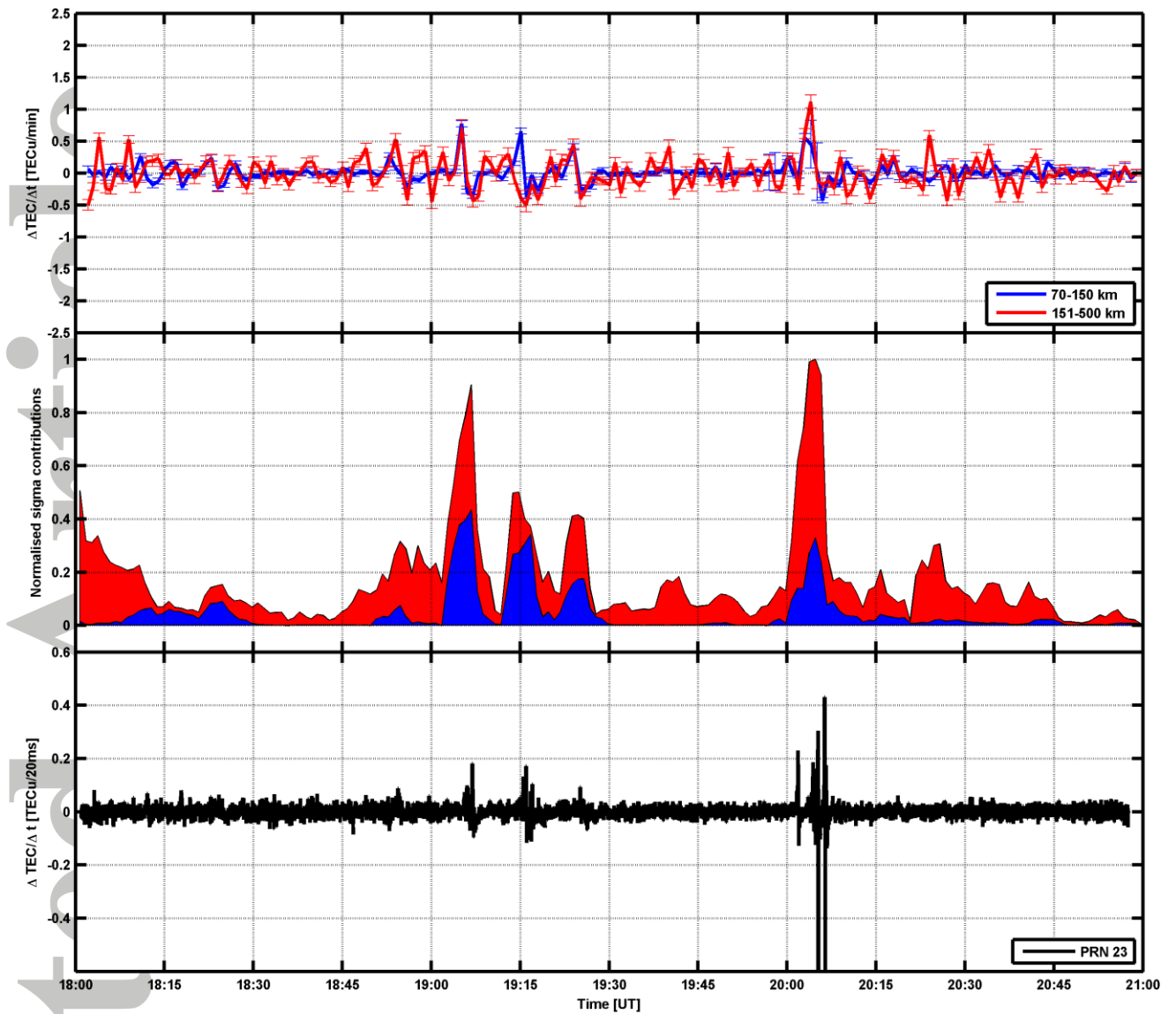
**Figure 4:** Magnetograms (variations in HDZ components in nT) from the IMAGE network (17 October 2013) from stations Ny Alesund (NAL), Hornsund (HOR), Bear Island (BJN), Tromso (TRO), Abisko (ABK), Jackvik (JCK).

Accepted

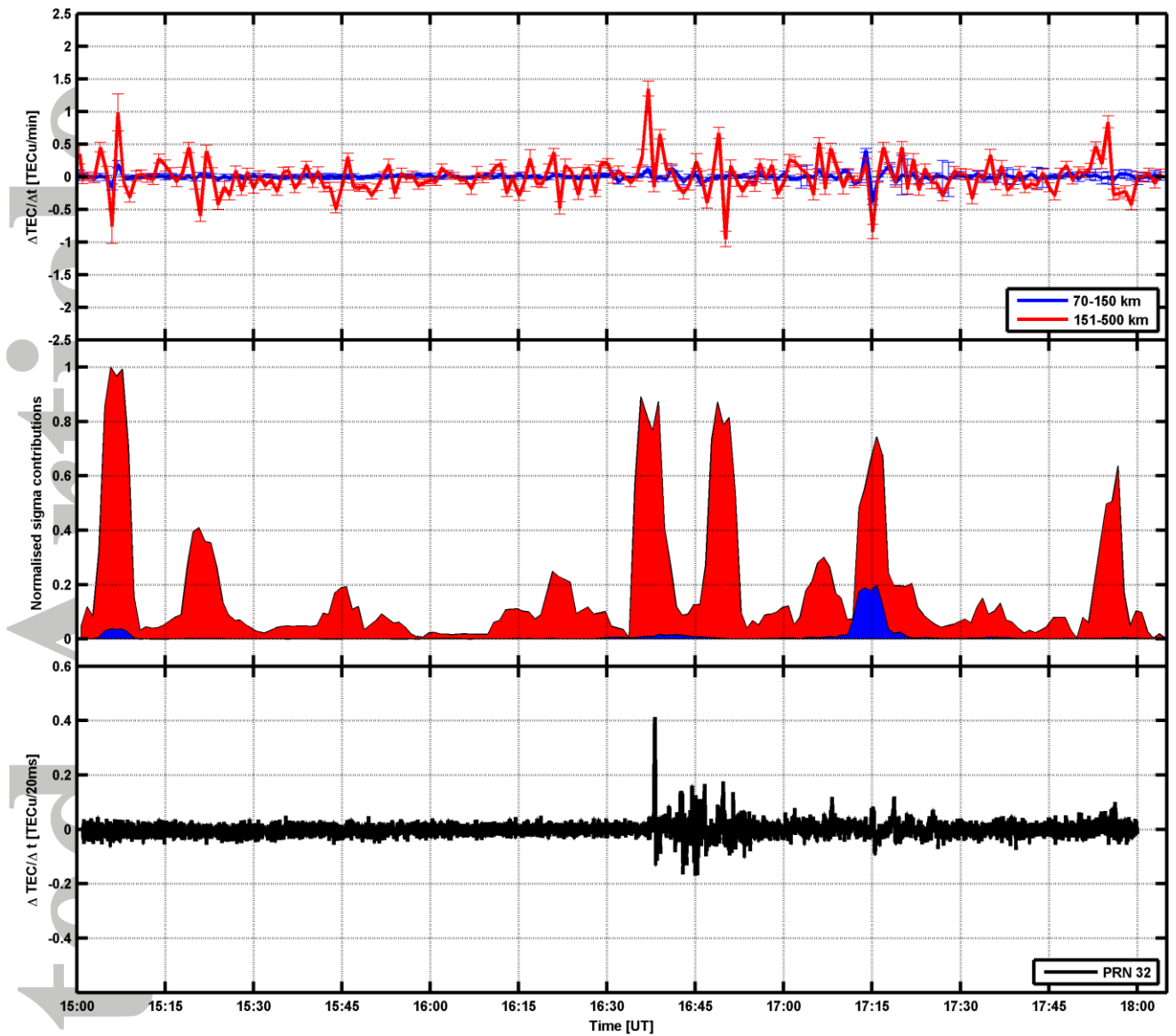


**Figure 5:** Magnetograms (variations in HDZ components in nT) from the IMAGE network (16 October 2013) from stations Ny Alesund (NAL), Hornsund (HOR), Bear Island (BJN), Tromso (TRO), Abisko (ABK), Jackvik (JCK)..

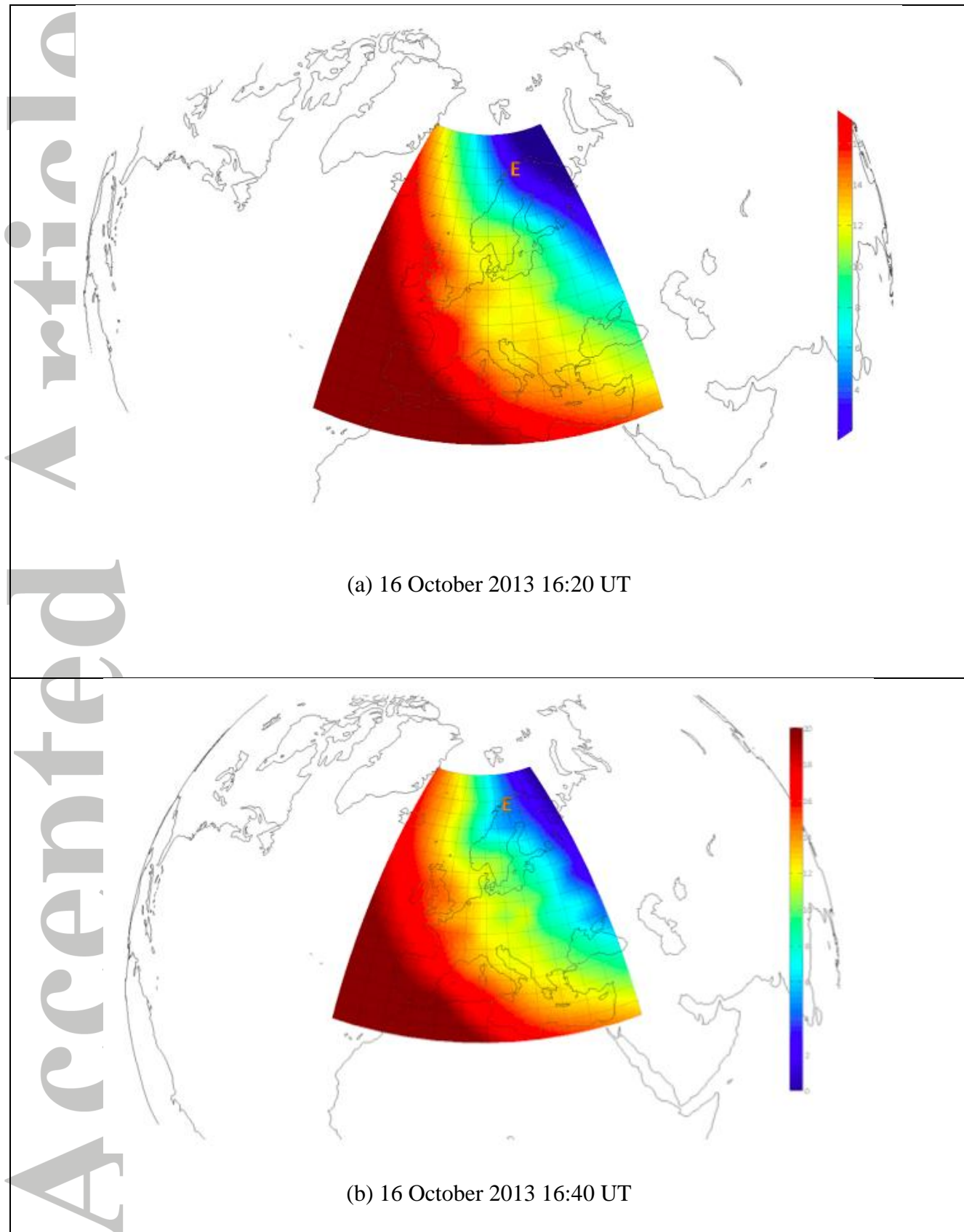
Accepted

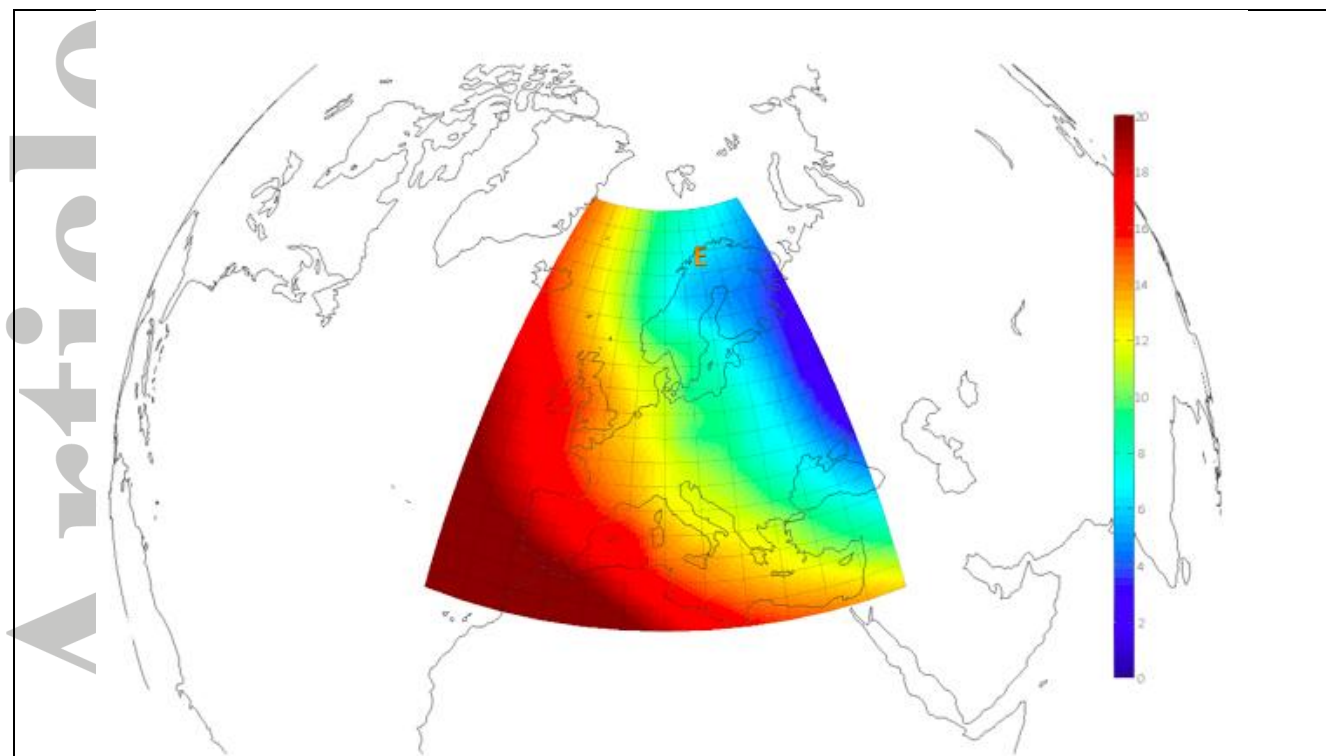


**Figure 6:** The event measured on 17 October 2013. Top: temporal fluctuations in the radar TEC obtained integrating EISCAT electron profiles for the E region (blue line) and the F region (red line), with error bars. Middle: the phase fluctuations originated from the E region (blue line) and the F region (red line). Bottom: the 50-Hz TEC temporal fluctuations on PRN32.

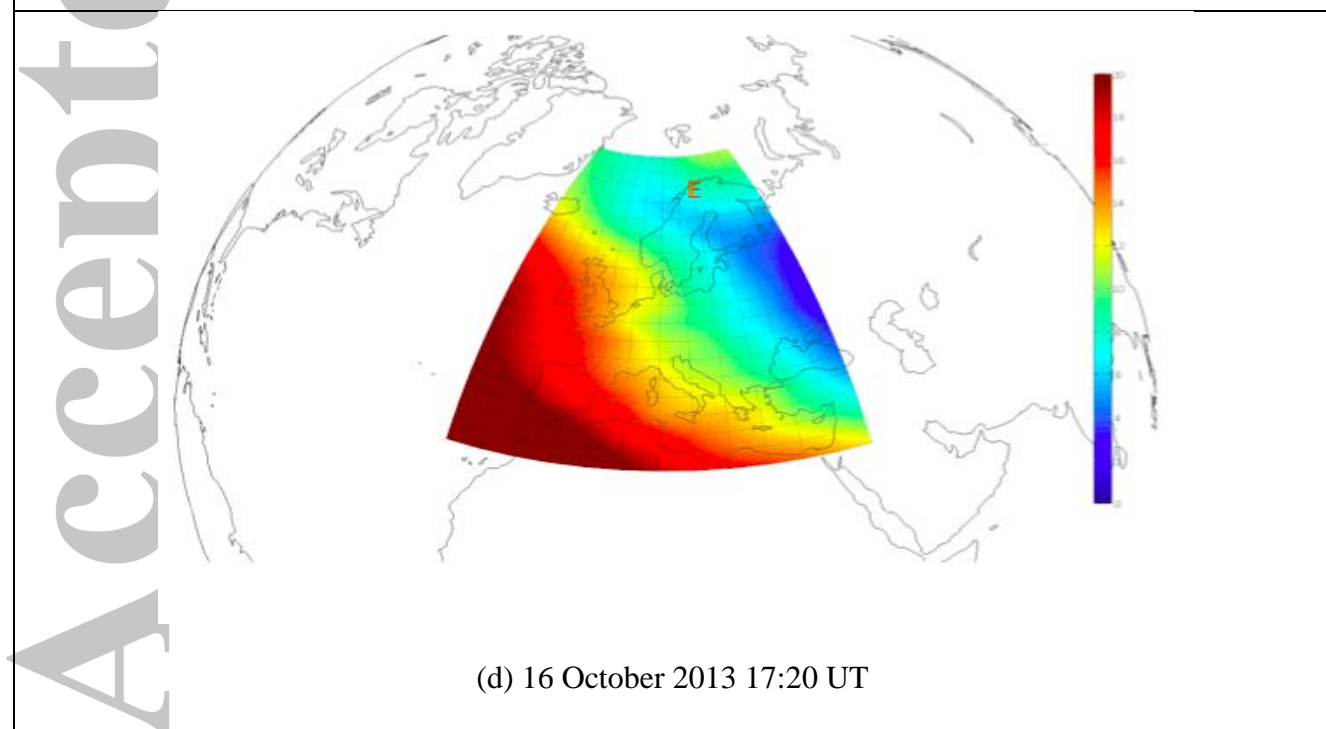


**Figure 7:** The event measured on 16 October 2013. Top: temporal fluctuations in the radar TEC obtained integrating EISCAT electron profiles for the E region (blue line) and the F region (red line), with error bars. Middle: the phase fluctuations originated from the E region (blue line) and the F region (red line). Bottom: the 50-Hz TEC temporal fluctuations on PRN23.





(c) 16 October 2013 17:00 UT



(d) 16 October 2013 17:20 UT

**Figure 8:** TEC maps reconstructed by tomographic imaging for 16 October 2013 between 16:20 and 17:20 UT. The trough forms south of Tromso between 16:40 and 17:20 UT. The location of the EISCAT radar close to Tromso is marked as 'E.' The trough can be recognised by the blue region indicating low TEC values extending across the EISCAT radar site between 16:40 and 17:20 UT.

Accepted Article

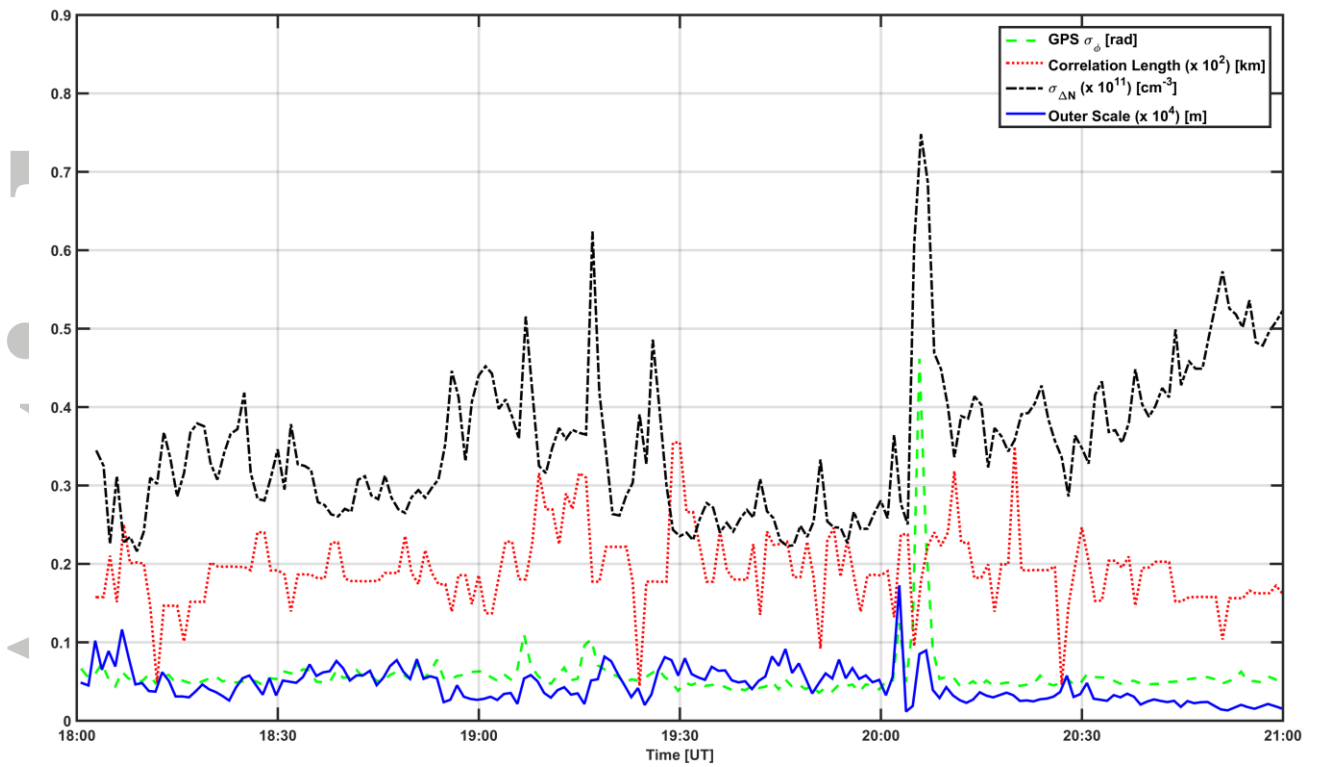


**Figure 9:** Estimate of propagation conditions on 17 October 2013: GPS phase scintillation index (green), standard deviation of electron density fluctuations along the line of sight (black), correlation length of ionisation structures (red), outer scale along the propagation direction (blue).

Accepted

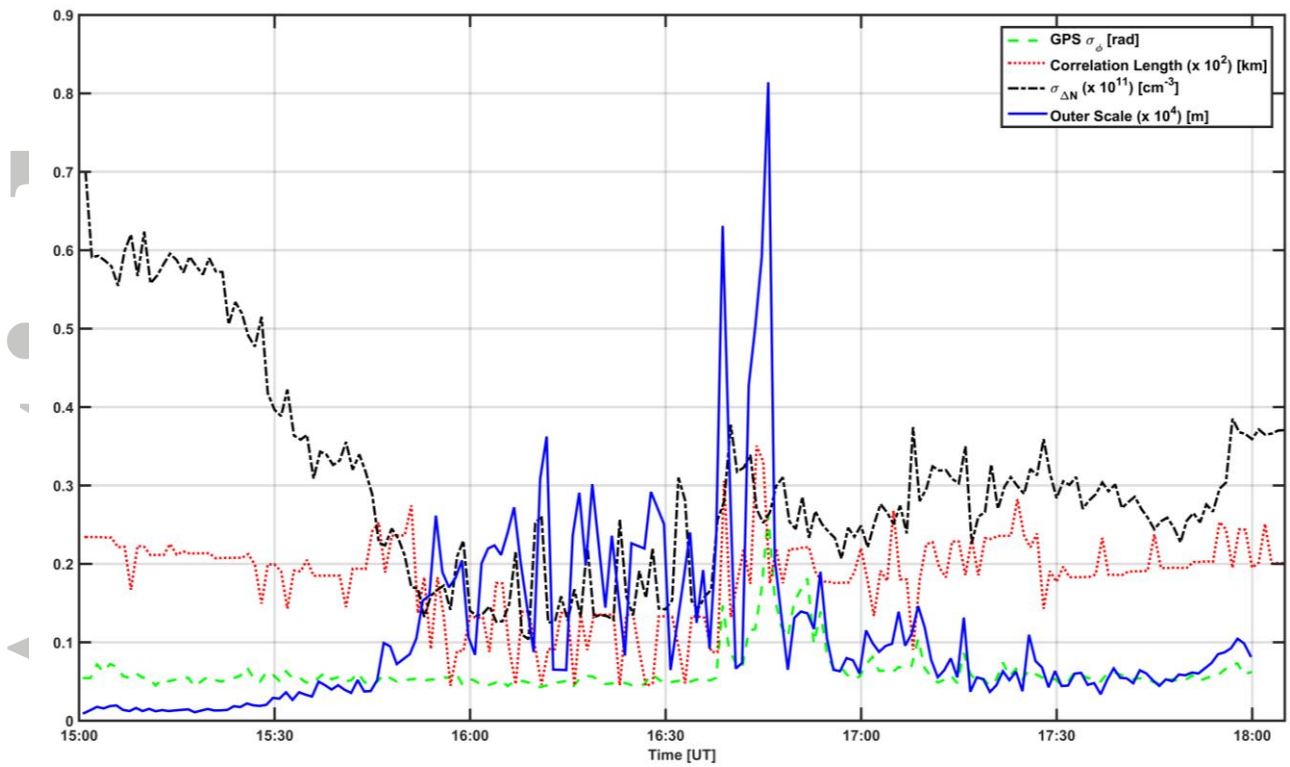


**Figure 10:** Estimate of propagation conditions on 16 October 2013: GPS phase scintillation index (green), standard deviation of electron density fluctuations along the line of sight (black), correlation length of ionisation structures (red), outer scale along the propagation direction (blue).

Accepted